

First Principles Modeling of the Initial Stages of Organic Solvent Decomposition on $\text{Li}_x\text{Mn}_2\text{O}_4$ (100) Surfaces

Kevin Leung

Sandia National Laboratories, MS 1415,

Albuquerque, NM 87185

kleung@sandia.gov

(Dated: September 18, 2012)

Abstract

Density functional theory and *ab initio* molecular dynamics simulations are applied to investigate the initial steps of ethylene carbonate (EC) decomposition on spinel $\text{Li}_{0.6}\text{Mn}_2\text{O}_4$ (100) surfaces. EC is a key component of the electrolyte used in lithium ion batteries. We predict a slightly exothermic EC bond breaking event on this oxide facet, which facilitates subsequent EC oxidation and proton transfer to the oxide surface. Both the proton and the partially decomposed EC fragment weaken the Mn-O ionic bonding network. Implications for interfacial film made of decomposed electrolyte on cathode surfaces, and $\text{Li}_x\text{Mn}_2\text{O}_4$ dissolution during power cycling, are discussed. keywords:

lithium ion batteries; lithium manganate; ethylene carbonate; density functional theory; *ab initio* molecule dynamics; computational electrochemistry

I. INTRODUCTION

Lithium ion batteries (LIB) featuring transition metal oxide cathodes and organic solvent-based electrolytes are currently the energy storage devices used to power electric vehicles. The high operational voltages of LIBs allow them to store significant amount of energy. However, these voltages can also induce electrochemical side reactions at electrode-electrolyte interfaces.^{1–3} These lead to irreversible capacity loss, power fade, durability, and safety issues. Understanding and controlling these interfacial reactions are of great interest for improving electric vehicles.

In this work, we focus on the basic science of one such reaction, and apply first principles computational techniques to study the first steps of ethylene carbonate (EC) decomposition on the (100) surface of spinel $\text{Li}_x\text{Mn}_2\text{O}_4$ used as the cathode material in many lithium ion batteries.^{4–7} EC (Fig. 1) is an indispensable electrolyte component for batteries that rely on graphitic carbon anodes. At the negative voltages needed to charge up a battery and intercalate Li^+ into graphite, EC-containing electrolyte decomposes to form stable solid-electrolyte interphase (SEI) films that prevent further electron leakage to the electrolyte.^{1–3} As such, substantial theoretical work has been devoted to excess electron-induced EC chemical reactions in the vicinity of the anode.^{8–13} One may argue that its ubiquity and critical role make EC in LIB the battery equivalent of the H_2O molecule in biology, geochemistry, and many solid-liquid interfacial science disciplines. The present work is indeed modeled after theoretical studies on water-on-mineral surfaces.^{15–18}

Oxidative reactions of organic electrolytes on cathode surfaces and formation of surface film from electrolyte decomposition products there^{19–53} are arguably less well understood than reduction on anode surfaces, especially at the atomic lengthscale. Electrolyte decomposition products such as LiF,²⁸ acetone,¹⁹ aldehydes,³¹ carbon dioxide,^{20,21,31} organic radicals,²⁷ and unidentified polymer, polyether, and carboxylic acid species^{22,24–26,34} have been detected either in gas form or on the surfaces of $\text{Li}_x\text{Mn}_2\text{O}_4$, as well as on Li_xCoO_2 and noble metal electrodes set at voltages comparable to those of $\text{Li}_x\text{Mn}_2\text{O}_4$. The salt used in the electrolyte strongly affects the surface film composition and properties.^{22,23,32,49,51,52} For example, LiPF_6 yields fluorine compounds that slow down Li^+ transport into the cathode.^{28,32}

The electrode is also degraded by side reactions. After cycling power, $\text{Li}_x\text{Mn}_2\text{O}_4$, exhibits surface morphology changes and loss of Mn and oxygen ions.^{4–6,28,32,36,37,39–41,43,45,51,52}

It has been widely accepted that Mn(III) ions on spinel electrode surfaces disproportionate into Mn(IV) and Mn(II),⁵⁴ the latter of which dissolves into the electrolyte. The presence of acid has been shown to facilitate dissolution and cathode degradation.⁵ In organic solvents, acid has been speculated to come from reactions between PF_6^- and trace water,⁴¹ or from organic solvent decomposition products themselves.³² Counterions other than PF_6^- cause slower Mn_2O_4 dissolution.^{32,41} There is also evidence that the emergence of proton-intercalated surface regions⁴¹ or other surface phases,⁴³ not just the loss of Mn active mass from the electrode, is responsible for cathode capacity loss. Dissolved Mn ions have been shown to diffuse to the anode, degrading the SEI there and weakening anode passivation.^{49–53} Thus anode and cathode degradation are closely related. Despite these key insights from experimental efforts, the free energy changes, activation barriers, specific surface configurations, and reaction pathways associated with Mn(II) dissolution have not been elucidated in organic electrolytes.

On the computational side, studies have focused either on cathode oxide surfaces without solvent molecules,^{55–59} or on anions^{60,61} or EC^+/PC^+ (with an electron removed) in the absence of the oxide.^{62–66} In studies of oxide-vacuum interfaces,^{55–59} it has been shown that under-coordinated Mn ions on Mn_2O_4 surfaces adopt low oxidation states, and these Mn have been argued to be susceptible to dissolution.⁵⁶ However, dissolution likely require that solvent molecules first directly coordinate to surface Mn ions,⁶⁷ which restores part of the octahedral coordination environment. When this happens, it is not obvious that the surface Mn(II) and Mn(III) ions do not revert back to Mn(IV). Explicit inclusion of solvent molecules on electrode surfaces would be extremely useful to investigate conjectures about surface Mn charge states.⁶⁸

The oxidation potentials of EC (and the similar PC)⁶² and electrolyte anions^{60,61} such as PF_6^- have been computed using DFT methods. These calculations assume a bulk liquid environment described by a dielectric constant ϵ_o , and an intact EC molecule (no ring opening reactions during oxidation). The predicted oxidation potentials are at least 1.5 V above the maximum voltage of 4.3 V applied in many electrolyte oxidation experiments for undoped spinel $\text{Li}_x\text{Mn}_2\text{O}_4$,^{22,27,31,32,47} in broad agreement with tabulated data obtained using inert electrodes.³ Recently, intriguing theoretical studies have predicted that PF_6^- or ClO_4^- in the vicinity of PC, with ϵ_o reduced to reflect “near-electrode” conditions, lowers the PC oxidation potential and leads to novel low-barrier reaction pathways.^{65,66} The anions

act as proton shuttles and/or provide fluorine atoms to react with PC. The oxidation steps are accompanied by bond-breaking events, which occur spontaneously during geometry optimization of (say) the $[EC/PF_6^-]^+$ pair. However, the predicted redox potential of this pair (4.94 V) remains higher than 4.3 V even after the local ϵ_o is set to unity.⁶⁶ This suggests that the electrode surface plays a role in catalyzing electrolyte decomposition. Despite the assumption of the proximity of the cathode, the electrode itself is not explicitly included in the calculations. Nevertheless, the predicted reaction mechanisms successfully reproduces organic products observed in experiments.⁶⁵

In the present work, the effect of $Li_{0.6}Mn_2O_4$ electrodes on EC oxidative decomposition is explicitly considered at the atomic lengthscale. The $x = 0.6$ Li content is roughly at the halfway point of charging or discharging. Our focus is on the initial reactions that modify and coat the oxide surface, not on the final distribution of gas/organic products. Our calculations do not extend to the high voltage region which seems to be required for CO_2 , one of the proposed final products.³⁷ Given the inevitable mixture of crystal facet/termination in battery cathode materials and the myriad effects of applied voltage, state-of-charge (lithium content), temperature, electrode cracking, sweep rate, presence of conductive carbon black, dissolution of surface films formed by electrolyte decomposition, and interference from salts, contaminants, and even processes at the anode, adopting all experimental conditions to these theoretical calculations is extremely difficult. Instead, we take a basic science starting point and focus on EC breakdown on defect-free $Li_{0.6}Mn_2O_4$ (100) surfaces. Our predictions can potentially be verified with experiments conducted under ideal conditions, but the mechanism predicted and insights obtained may still be relevant to battery conditions and may motivate new experiments and interpretations of battery degradation processes.

Our approach resembles the intensive study of H_2O adsorption on rutile (011),¹⁵ anatase (101),^{16,17} anatase (001),¹⁷ and many other surface facets of technologically important titanium oxide over more than a decade. As in the case of water-oxide interfaces, both ultra-high vacuum (UHV) and liquid-immersed electrode conditions are considered in our interfacial models. These conditions yield qualitatively similar predictions. Like H_2O on some TiO_2 facets, EC is found to chemisorb on $Li_xMn_2O_4$ (100), breaking internal covalent bonds in the process. This initial decomposition step enables the subsequent oxidation reaction which involves electron and proton transfer to the oxide surface. This suggests that organic solvent decomposition and Mn_2O_4 dissolution may be related. No assumption of a local ϵ_o is needed

in our calculations.

The (100) surface has been the focus of most theoretical studies on spinel $\text{Li}_x\text{Mn}_2\text{O}_4$.^{55,56,67} Although the (111) surface is most prominent in LiMn_2O_4 particles,⁶⁹ (100) facets remain even after annealing at 800 °C for 100 hours.⁶⁹ The (100) surface has also been synthesized directly on strontium titanate substrates.⁴⁰

This work is organized as follows. Section 2 describes the theoretical method used. Section 3 discusses EC decomposition on $\text{Li}_{0.6}\text{Mn}_2\text{O}_4$. Further discussions in Sec. 4 put the results on ideal model surfaces in the context of battery operating conditions and provide more comparison with the theoretical literature. Sec. 5 recapitulates the key findings, and two appendices describe the charge states of the Mn ions and the reactions of H_2O contaminants and hydroxyl groups on $\text{Li}_x\text{Mn}_2\text{O}_4$ (100) surfaces.

II. METHODS

Static ($T=0$ K) DFT+U and finite temperature *ab initio* molecular dynamics (AIMD)⁷⁰ simulations are conducted under UHV and solvent-immersed electrode conditions, respectively.

The majority of the calculations are performed using the Vienna Atomic Simulation Package (VASP) version 4.6^{71,72} and the PBE functional.⁷³ Modeling spinel $\text{Li}_x\text{Mn}_2\text{O}_4$ requires the DFT+U augmented treatment⁷⁴ of Mn 3d orbitals. The U and J values depend on the orbital projection scheme and DFT+U implementation details; here $U - J = 4.85$ eV is chosen in accordance with the literature.⁷⁵ A few PBE0 hybrid DFT functional⁷⁶ calculations are also performed using VASP version 5.2.⁷⁷ This more costly method is meant to provide spot checks of DFT+U results. A 400 eV planewave energy cutoff is imposed in all cases.

Static geometry optimization and climbing image nudged elastic band (NEB)⁷⁸ barrier calculations are performed using a 10^{-4} eV convergence criterion and $1 \times 2 \times 2$ Brillouin zone sampling. The simulation cells are of $27.59 \times 8.40 \times 8.40 \times \text{\AA}^3$ dimensions and have a $\text{Li}_6\text{Mn}_{20}\text{O}_{40}$ stoichiometry, not counting the EC molecule. The bare lithiated spinel slab is generated as follows. A (100) $\text{Li}_{10}\text{Mn}_{20}\text{O}_{40}$ surface slab is relaxed to its optimal geometry. The predicted 0.69 J/m² surface energy agree with the literature value.⁵⁵ To reach the target stoichiometry, 4 Li atoms need to be removed. There are 210 possibilities, many of which are related by symmetry. The lowest energy configuration (Fig. 2) is found to be the one

where a Li on each surface and half (two) of the Li atoms in the middle layer of the slab are removed. The lattice constants are kept at those of LiMn_2O_4 . A larger system, $\text{Li}_8\text{Mn}_{24}\text{O}_{48}$, is also discussed in appendix A.

AIMD simulations feature $40 \times 11.88 \times 11.88 \text{\AA}^3$ simulation cells with a $\text{Li}_{12}\text{Mn}_{40}\text{O}_{80}$ oxide slab generated by expanded the oxide slab used in static calculations twofold. 32 EC molecules are confined between the two surfaces of the slab in the periodically replicated simulation cell. Γ -point Brillouin zone sampling and a 10^{-6} eV convergence criterion are applied at each Born-Oppenheimer time step. The trajectories are kept at an average temperature of $T=450$ K using Nose thermostats. Tritium masses on EC are substituted for protons to permit a time step of 1 fs. Under these conditions, the trajectories exhibit drifts of less than 2 K/ps. EC configurations are pre-equilibrated using Monte Carlo simulations and simple molecular force fields, as described in an earlier work.¹¹ We also report AIMD simulations of hydroxylated MnO_2 surfaces in appendix B, using deuterium masses for H atoms and a 0.5 fs time step there.

AIMD potential-of-mean-force (PMF, denoted as $W(R)$ hereafter) calculations apply composite reaction coordinates of the form $R=R_1-R_2$. R covers the first two steps of the reaction. R_1 and R_2 are the distances between the O_E and C_C atoms and between C_C and O_1 (on the oxide surface), respectively (Fig. 1). In the next step, we apply another composite coordinate $R'=R'_1-R'_2$, where R'_1 and R'_2 are the distances between H and C_E , and between H and O_2 , respectively (Fig. 1). Harmonic potentials of the form $B_o(R - R_o)^2$ and a series of 10 windows with a progression of R_o values span the reaction path R . B_o ranges from 2 to 4 eV/ \AA^2 . Less windows are used along the R' coordinate. The statistical uncertainties in $W(R)$ and $W(R')$ are estimated by splitting the trajectory in each window into four, calculating the standard deviation, and propagating the noise across windows assuming gaussian statistics.

To determine Mn charge states, we examine the electron spin on each Mn ion demarcated according to PAW orbital projections.⁷² All calculations allow unconstrained spin polarization. Bulk LiMn_2O_4 crystal is antiferromagnetic (AFM). We have imposed an AFM ordering on alternate Mn planes along the (011) direction. The bare spinel surface slab is also AFM.

III. RESULTS

A. Gas phase energetics

The DFT/PBE functional predicts that gas phase disproportionation of ethylene carbonate into carbon dioxide and acetaldehyde,



is exothermic by 0.317 eV at T=0 K, not counting zero-point energy or finite temperature entropic effects which should further favor dissociation. This result is qualitatively consistent with a reported hybrid DFT predictions which however include entropy contributions.⁷⁹ We have not calculated the activation energy, but it must be high for metastable EC to be useful in battery operations. No electron is transferred in Eq. 1. The corresponding disproportionation products for PC would be CO₂ and acetone ((CH₃)₂CO). Therefore observation of CO₂ and acetone/acetaldehyde in experiments may not always arise from electrolyte oxidation, as was already pointed out.^{19,20} They could be also be the product of EC/PC catalytic decomposition on battery material surfaces.

B. Reaction intermediates

Next we consider the intermediates associated with EC decomposition on Li_{0.6}Mn₂O₄. Discussions of the activation barriers between them will be deferred to later sections.

Figure 2a (configuration “A”) depicts an intact EC physisorbed on the (100) surface. The carbonyl oxygen (O_C) is the only atom strongly coordinated to the oxide, and is 2.16 Å from one of the two surface Mn(IV) ions (among eight surface Mn, appendix A) in the simulation cell. The overall adsorption energy is 0.480 eV. This tilted EC geometry binds more strongly to the surface than one where EC is in upright. The overall magnetic polarization of the simulation cell is 2 μ_B . If a net zero spin polarization constraint is imposed, the total energy increases by only 0.040 eV. This underscores the fact the energy differences associated with spin flipping tend to be small.

In the first reaction intermediate B (Fig. 2b), the carbonyl carbon atom (C_C, Fig. 1) is subjected to nucleophilic attack by an oxygen atom on the surface, becoming 4-coordinated and *sp*³ hybridized. This bent EC species is reminiscent of the bent EC⁻ geometry during

method	A	B	C	D	E
DFT+U	0.000	-0.011	-0.100	-2.057	-2.144
PBE0	0.000	-0.107	-0.260	-1.911	NA

TABLE I: Energies of configurations A-D (Fig. 2), in eV, computed at T=0 K using different methods.

electrochemical *reduction* of EC at anode surfaces.¹⁴ However, a maximally localized Wannier function⁸⁰ analysis performed on this configuration reveals that the EC carries no net charge. The configuration change is slightly exothermic (Table I). Note that two types of oxygen ions exist on the (100) surface even in the absence of adsorbed EC: those bonded to an Mn ion on the subsurface layer, and those that are not. The latter are more reactive, and the EC adsorption configuration is chosen so that the C_C atom can bind to the latter type.

The next intermediate C (Fig. 2c) features one broken C_C-O_E bond, with the C_C atom now reverting to *sp*² hybridization. Both the O_E atom on the broken bond and C_C become coordinated to the surface while the carbonyl oxygen (O_C) is detached. The surface Mn ion bound to the O_E atom now has 6-ionic or covalent bonds and transitions from a +3 to a +4 charge state, with an 3*d* electron originally in its 3*d* shell migrating to a Mn(IV) on the surface (appendix A).

In Fig. 2d (product D), the proton on the C_E atom closest to the surface is transferred to a surface oxygen with a substantial gain in energy (Table I). Counting all Wannier orbitals centered closer to the EC C and O nuclei than Li_{0.6}Mn₂O₄ atoms as belonging to the EC fragment, EC now contains 32 valence *e*⁻, implying that two of its *e*⁻ have been transferred to the oxide (appendix A). The oxidized EC fragment contains a +33|*e*| pseudovalent nuclear charge and a +|*e*| net charge. This oxidative step is apparently facilitated by the preceding bond making/breaking events.

The proton-accepting O ion on the oxide surface is coordinated to 3 other Mn ions. The average Mn-O distance associated with this O atom becomes 2.13 Å, an increase of 0.14 Å from the value (1.99 Å) prior to proton transfer. Thus EC oxidation on the spinel oxide surface has led to significant weakening of the Mn-O ionic bond network on the Li_xMn₂O₄ surface. We argue that this may contribute to Mn(II) dissolution⁴¹ (see also appendix B).

Finally, as will be discussed in Sec. III D, the configuration in Fig. 2d spontaneously reorganizes during AIMD simulations of the liquid EC/Li_{0.6}Mn₂O₄ interface. An oxygen ion on

the oxide surface is pulled outwards, and the O_C atom re-coordinates to an adjacent surface Mn ion. Extracting the EC fragment configuration from an AIMD snapshot, transplanting it into the smaller UHV simulation cell to give a cell commensurate with those of Figs. 2a-d, and optimizing the geometry yield Fig. 2e, with a further 0.087 eV gain in energy. Thus all steps of the reaction are exothermic or approximately thermoneutral (Table I). The configuration in Fig. 2e maintains a $+|e|$ charge in both the T=0 K optimized geometry and the AIMD snapshot, counting only the electrons on the original C and O atoms of the EC.

DFT+U predictions depend on the value of U . This is especially a concern with the C→D reaction, a redox process accompanied by Mn charge state changes. The redox potentials of transition metal ion centers have been shown to depend on DFT functionals in some cases.^{81–84} Thus we have applied the widely used hybrid DFT functional PBE0, which carries no tunable parameters, to spot-check DFT+U results. The predicted exothermicities differ by less than 0.16 eV in all cases considered (Table I). In particular, the overall A→D redox reaction at T=0 K differ only by 0.15 eV. The good agreement shows that the results are not strongly dependent on DFT functionals, and gives us confidence in DFT+U-based predictions for our system.

C. Activation (free) energies: A to C

Figure 3 depicts the zero temperature energy profile connecting A (Fig. 2a) and B (Fig. 2b), computed using the climbing image NEB method. The barrier is 0.240 eV. This small barrier is substantially less than the endothermicity associated with the EC bending motion on hydroxylated LiAlO₂ surfaces,¹⁴ presumably because EC binds more strongly to Li_xMn₂O₄ (100).

The barrier between intermediates B and C has not been calculated at T=0 K. Instead, AIMD simulations of liquid EC/Li_xM₂nO₄ interfaces at finite temperature cover the A→C steps. But first we discuss unconstrained AIMD simulations of EC liquid confined between Li_xMn₂O₄ surfaces prior to any chemical reactions. Intact EC molecules have large dipole moments but are generally much more strongly coordinated to cations than anions. The 8 surface Mn ions are observed to be coordinated to between 2 and 7 EC molecules, where we have used the arbitrary but reasonable coordination criterion that Mn must be within 2.5 Å of one of the EC oxygen atoms. The mean value is 3.7 over the trajectory. As will

be shown, EC should decompose on a subsecond timescale on $\text{Li}_{0.6}\text{Mn}_2\text{O}_4$ (100). Therefore the distribution of intact liquid EC on the clean (100) surface is of academic interest.⁸⁵ The primary purpose of including the EC liquid is to provide a reasonable EC liquid solvation environment.

PMF calculations are initiated from the unconstrained trajectory. We start with a snapshot where an intact surface EC molecule exhibits an adsorption geometry resembling Fig. 2a. As mentioned in Sec. II, a composite reaction coordinate $R=R_1-R_2$ is applied, where R_1 is the distance between C_C and O_E and R_2 is that between C_C and O_1 on the surface (Fig. 1). If the simple coordinate $R = R_1$ is used, the EC tends to desorb from the surface during the AIMD trajectory before bond breaking can occur. If $R = R_2$, the reaction stops after configuration B is reached.

Figure 4a depicts the $W(R)$ computed using this composite coordinate. The minimum associated with intermediate B is less stable than the reactant by 0.24 ± 0.05 eV. This is less favorable than the -0.011 eV found at T=0 K (Table I). The barrier between A and B also increases to a still modest 0.48 ± 0.05 eV. The reason is most likely the entropy change which is included in $W(R)$ but not in Fig. 3a. The 4-coordinated intermediate B is evidently more constrained and entropically unfavorable than the loosely bound, flat EC molecule (Fig. 2a).

The AIMD-predicted barrier between intermediates B and C is smaller than that between A and B. The exothermicity between the $W(R)$ minima associated with C and A is -0.06 ± 0.06 eV, which is similar to the energy difference computed at T=0 K (-0.10 eV). Thus, the main conclusion is that the liquid EC environment does not qualitatively modify the conclusions obtained under UHV conditions.

D. Activation (free) energies: C to E

Figure 4a depicts the T=0 K energy profile between intermediates C and D. The reaction is exothermic by 1.957 eV and exhibits a 0.618 eV energy barrier. Ignoring entropic effects and assuming a typical molecular vibrational prefactor of $10^{12}/\text{s}$, such an enthalpic barrier permits a $18/\text{s}$ reaction rate. As a typical battery charging/discharging rate is 1 C (i.e., takes about an hour), the predicted subsecond reaction rate means that EC oxidation proceeds readily during battery operations.

Next we consider temperature/solvent effects. Figure 4b depicts the AIMD $W(R')$ for

this segment of the reaction. We apply a second composite reaction coordinate $R' = R'_1 - R'_2$, where R'_1 and R'_2 are the distances between H and C_E, and between H and O₂, respectively (Fig. 1a; Sec. II). The predicted liquid state $W(R')$ barrier (0.54 eV) is slightly smaller than the gas phase value (Fig. 4a). The overall reaction exothermicity may be higher in the presence of liquid EC than under UHV conditions because the product is charged and stabilized by the high dielectric liquid environment. As the barrier is the main object of interest, we have not extended $W(R')$ far into the product channel. It is sufficient to know that the reaction is strongly exothermic.

Note that the electron transfer from C to D occurs right at the electrode-solvent interface. It is distinct from the long-range electron transfer mechanism experienced by “outershell” ionic complexes in classic electrochemical studies, and should consequently be much less influenced by the electric double layer.

Configuration D spontaneously reorganizes to E (Fig. 2e) after a 2 ps AIMD trajectory. We have not computed the free energy barrier between these configurations, but it must be on the order of $k_B T$ for the conformation change to occur on such a short timescale.

E. Other products/intermediates are unfavorable

Fig. 5a depicts an otherwise intact EC molecule with a proton transferred to the oxide surface. Compared to the intact adsorbed EC (Fig. 2a), this configuration is endothermic by 0.398 eV. In contrast, removing a proton from the EC with a broken C_C-O_E bond (Fig. 2c) is exothermic by 2.057 eV overall. This shows that the non-oxidative, bond-breaking first steps strongly facilitate redox reactions on the spinel surface.

Several possible decomposition products, devised from breaking a C_E-O_E bond at various stages of the reaction, lead to higher total energies and/or high barriers and are ruled out. In Fig. 5b, we attempt to break a C_E-O_E bond in the Fig. 2a configuration to form a carbonate-like group in the first reaction step. The optimized metastable geometry is unfavorable by 1.562 eV compared to the physisorbed, intact EC (Fig. 2a).

Fig. 5c depicts a configuration resulting from cleaving a C_E-O_E bond in Fig. 2c without first transferring a proton to the surface. One product fragment, a acetaldehyde molecule which arises from internal proton transfer among the carbon atoms in the CH₂CH₂O fragment, is detached from the surface, while the other, a CO₂ molecule, remains strongly

coordinated to the metal oxide. No electron is transferred. This configuration is exothermic by 0.646 eV compared to the intact physisorbed EC, but is much less stable than that in Fig. 2d. (See also Sec. III A.) We have not found a converged barrier smaller than 1.5 eV for this reaction. Hence the Fig. 2d product channel is much more favorable.

Figure 5d explores the possibility of C_E-O_E bond-breaking following proton transfer (Fig. 2d). The resulting product is far less stable than if the C_E-O_E bond remains intact (Fig. 2d).

In conclusion, we have not found a favorable reaction pathway that yields CO_2 and/or acetaldehyde-like fragments. This suggests that the partially decomposed EC fragments chemisorbed on the (100) surface (Fig. 2d & 2e) is stable under UHV conditions. Preliminary AIMD PMF simulations also show that breaking a EC bond in configuration D (Fig. 2d) or configuration E (Fig. 2e) to Fig. 5d exhibits large barriers.

However, the chemisorbed EC fragment (Fig. 2e) can potentially attack and react with other intact solvent molecules, potentially abstracting protons and/or electrons (“ H^- ”) from them. This has not been observed in our AIMD simulations which are of limited duration. In view of Refs. 65 and 66, it is also possible that further decomposition of the fragment can occur in the vicinity of anions in the electrolyte, which can act as proton shuttles.

IV. DISCUSSIONS

A. Relevance to battery operating conditions

Our calculations focus on the clean $Li_xMn_2O_4$ (100) surface, which has been the focus of almost all theoretical studies.^{56,67} Thin Li_2CO_3 films are known to exist on cathode oxide surfaces before cycling power.^{29,34} Since electrolyte decomposition products are observed on these oxides surfaces, it has been suggested that this film dissolves upon immersion in the electrolyte, during or prior to cycling power.^{28,39,40}

The reaction products and pathways reported on (100) are not meant to quantitatively reproduce all experimental spinel facets present. If the adsorbed, partially decomposed EC^+ fragments (Fig. 2d,e) on $Li_{0.6}Mn_2O_4$ (100) are stable, they become part of the cathode surface film and may interfere with Li^+ intercalation. These products block the reactive sites, of surface concentration $1/17.6 \text{ \AA}^2$, but do not form a continuous film to stop electron

tunneling from the cathode to the electrolyte.

The fact that PF_6^- is found to accelerate Mn_2O_4 degradation is not inconsistent with our findings. PF_6^- may further react with, decompose, and removed the chemisorbed EC^+ fragments on the surface (Fig. 2e) to form volatile organic products.⁶⁵ This may expose reactive sites on the oxide surface, allowing other EC molecules to react and potentially deposit more protons. This will be considered in the future. The $\text{H}_2\text{O}/\text{PF}_6^-$ pathway discussed in the literature may also occur simultaneously with our predicted EC H⁺-donation mechanism.

As no counter electrode is present in the simulation cell, our AIMD simulations represent an open-circuit condition with a $\text{Li}_{0.6}\text{Mn}_2\text{O}_4$ stoichiometry which may be more related to battery storage than charging experiments. For larger values of x , Mn(IV) has less tendency to reside on the oxide surface, and the reactivity of EC should decrease. This may be consistent with the observation that higher charging voltages yield more interfacial reactions.^{36,37}

B. Comparison with EC^+/PC^+ decomposition predictions made in the absence of an electrode

To some extent, our proposed EC decomposition mechanism (Fig. 2a-e) is the reverse of that of Refs. 65 and 66. Oxidation and proton removal from EC occur in the last, not first, step. A C-O bond first ruptures on a EC initially physisorbed the $\text{Li}_x\text{Mn}_2\text{O}_4$ surface, facilitating subsequent redox reactions.

As in this work, Refs. 65 and 66 emphasize the role of proton removal from organic solvent molecules during oxidation. All these studies suggest that trace water may not be needed to initiate degradation of the cathode by creating acid molecules. The final products reported in Ref. 65 (which does not consider explicit electrodes) are coordinated to anions. In our work, anions are not present, and similar products are at best metastable.

We predict preferential cleavage of the $\text{C}_\text{C}-\text{O}_\text{E}$ bond, not $\text{C}_\text{E}-\text{O}_\text{E}$, in agreement with Xing *et al.*'s results on the decomposition of isolated EC^+ and PC^+ .^{63,64} The final products predicted by Xing *et al.* are not observed because EC oxidation is accompanied by proton transfer to the surface herein.

C. More discussions on computational methods

e^- transfer between the EC and Mn ions, and between Mn ions, are implicitly assumed to exhibit lower barriers than the rate-determining step in the bond-breaking processes. This follows from the DFT (and DFT+U) calculations, where e^- transfer events are implicitly assumed to adiabatically follow ionic trajectories. Non-adiabatic effects are not expected to dominate, because non-adiabatic polaron transport in spinel Mn_2O_4 are not predicted to exhibit high barriers.⁹⁰ The e^- transfer between configurations C (Fig. 2c) and D (Fig. 2d) is unlikely to be rate limiting either, because the partially decomposed EC molecule is covalently bonded to the surface, yielding robust e^- conduction pathways. While hybrid functionals are generally more accurate than DFT+U for the C→D reaction which involves concerted electron and proton transfer, we have found that both methods predict similar energy changes (Table I).

Zero point energy (ZPE) are not included in the energy changes reported in this work. Most bond-breaking events examined involve “heavy” second row atoms. In some cases, a proton is transferred from a carbon to an oxygen atom. As C-H and O-H vibrational frequencies are within 20% of each other, ZPE should not strongly modify the predicted exothermicities. Proton transfer barriers would be even lower if ZPE is included.

Finally, we mention that the reaction pathway (Fig. 2) is chosen through trial and error. A more systematic approach would be to apply metadynamics.^{86–88} The transition path sampling approach can also be combined with AIMD simulations to yield more rigorous free energy barriers.⁸⁹

V. CONCLUSIONS

This computational work focuses on the initial stages of ethylene carbonate (EC) decomposition on $Li_{0.6}Mn_2O_2$ (100) surfaces. In analogy with studies of water adsorption and dissociation on transition metal oxide surfaces, we perform calculations on clean, ideal surface models that can potentially be replicated in future experiments. Both ultra-high vacuum (UHV) and solvent-immersed electrode conditions are considered. Static ($T=0$ K) DFT calculations and finite temperature *ab initio* molecular dynamics (AIMD) simulations are applied under these conditions, respectively, yielding qualitatively similar conclusions.

The first step of EC decomposition on $\text{Li}_{0.6}\text{Mn}_2\text{O}_4$ involves $\text{C}_C\text{-O}_E$ bond-cleavage but no oxidation. This slightly exothermic bond-breaking event enables a proton and two electrons to be transferred to the oxide surface in the next oxidative, strongly exothermic step. The activation energies for both steps are about 0.62 eV under UHV conditions and 0.54 eV at electrode-electrolyte interfaces, according to our DFT+U calculations. Thus oxidation of EC on the (100) surface is predicted to take place on a subsecond timescale. The Mn-O ionic bonding network is weakened by the EC proton transferred to the surface as well as the adsorbed EC fragment, suggesting that solvent decomposition and Mn and/or O dissolution from the oxide surface may be related. The fact that proton can come from organic solvents has been suggested by an experiment work using tetrahydrofuran.³² Our work suggests a surface-assisted pathway for solvent oxidation and surface film formation at the open circuit $\text{Li}_{0.6}\text{Mn}_2\text{O}_4$ voltage. No assumption or separate calculation of spatial inhomogeneity effect on the local dielectric constant is made in this work.

The predicted EC fragment chemisorbed on the oxide (100) surface is likely not the final product. Our goal is not to reproduce the final distribution of organic decomposition products observed in battery experiments. In particular, our calculations do not extend to the high voltage region which seems to be required for CO_2 , one of the proposed final products.³⁷ Instead, this work represents the perhaps necessary first step of explicit modeling of electrolyte breakdown on oxide surfaces, and paves the way for theoretical and experimental investigations on other $\text{Li}_x\text{Mn}_2\text{O}_4$ crystal facets.

Acknowledgement

We thank Nancy Missett, Nelson Bell, Yue Qi, Steve Harris, Kevin Zavadil, and John Sullivan for useful discussions. Solid state LiMn_2O_4 calculations are initiated using a unit cell provided by Shirley Meng. Sandia National Laboratories is a multiprogram laboratory managed and operated by Sandia Corporation, a wholly owned subsidiary of Lockheed Martin Corporation, for the U.S. Department of Energy's National Nuclear Security Administration under contract DE-AC04-94AL85000. UHV-condition calculations were supported by Nanostructures for Electrical Energy Storage (NEES), an Energy Frontier Research Center funded by the U.S. Department of Energy, Office of Science, Office of Basic Energy Sciences under Award Number DESC0001160. This research used resources of the National Energy

Research Scientific Computing Center, which is supported by the Office of Science of the U.S. Department of Energy under Contract No. DE-AC02-05CH11231.

Appendix A: Charge states of Mn ions

In Sec. III B, changes in Mn charge states within the oxide slab are briefly discussed. They are explicitly depicted in this appendix. Fig. 6a shows that 6 Mn(III) and 2 Mn(IV) ions in the $\text{Li}_6\text{Mn}_{20}\text{O}_{40}$ slab reside on the (100) surface. The physisorption of an intact EC on a surface Mn(IV) ion does not change this charge state distribution (Fig. 6b). Upon breaking an EC C-O bond, however, the O atom on that broken bond becomes strongly bound to a surface Mn ion, which loses an electron to the adjacent, formerly Mn(IV) ion on the surface (Fig. 6c). The oxidative step transfers two e^- to the oxide slab. As a result, both a surface and an interior Mn(IV) turn into Mn(III) (Fig. 6d).

The possibility of an EC adsorbed on a surface Mn(III) ion is also considered. Upon optimizing the Kohn-Sham wavefunctions and the geometry, the Mn(III) coordinated to the EC carbonyl oxygen reverts to an Mn(IV), with the extra electron migrating to another surface Mn(IV), converting that Mn to a Mn(III) (not shown). This suggests that the charge states of surface Mn ions strongly depend on whether molecules are coordinated to them, at least on this (100) surface.

We have also considered a larger, $\text{Li}_8\text{Mn}_{24}\text{O}_{48}$ slab, of the same lateral dimension as the $\text{Li}_6\text{Mn}_{20}\text{O}_{40}$ model studied in most of this work. The tetrahedral site occupancies are determined by calculating the energies of all symmetry-distinct Li-configurations. This model features 8 Mn(III) ions, and in principle all 8 surface Mn could have been Mn(III). Instead, 2 of the 8 surface Mn remain Mn(IV), presumably because the surface layers are deficient in Li^+ .

Appendix B: Hydroxyl and proton on (100) spinel MnO_2 surface

Interactions between H_2O and $\text{Li}_x\text{Mn}_2\text{O}_4$ surfaces are pertinent to how trace H_2O in the atmosphere or electrolyte affects Mn_2O_4 stability. (Water may also emerge from electrolyte decomposition.) Acids are known to degrade spinel oxide electrodes,^{5,68} and water can be a source of H^+ . In this appendix, we consider the effect of decorating and functionalizing

$\text{Li}_x\text{Mn}_2\text{O}_4$ (100) surfaces with H_2O , H^+ , and OH^- groups.

Figure 7a depicts H_2O physisorption on the (100) surface at the $x = 0.6$ stoichiometry. It exhibits a binding energy of 0.452 eV, comparable to EC physisorption. Breaking a O-H bond in water and displacing the proton to a neighboring surface O ion to form two new hydroxyl groups lead to a 1.027 eV binding energy after performing geometry optimization (Fig. 7b). Thus dissociative chemisorption is more favorable than physisorption by 0.575 eV. However, even this chemisorbed configuration may be metastable compared to one where the H^+ has penetrated into the subsurface layer (see below).

Next, we consider the effect of multiple hydroxyl groups on the surface. We turn to Mn_2O_4 , without Li^+ intercalation, and decorate all surface O ions with H atoms and all surface Mn ions with OH groups. The geometry is relaxed to a local energy minimum (Fig. 7c). The first type of hydroxyl groups, originating from protonation of surface oxygen atoms, point outward or parallel to the oxide surface. The second type, hydroxyl groups formed by adding OH pendants to Mn, always point out of the plane. As there are more added H than OH, the charge-neutral slab now contains some Mn(III) ions.

Starting from this optimized geometry, a 11 ps AIMD trajectory is conducted at T=450 K. The final configuration is shown in Fig. 7d. Some type 1 hydroxyl groups now point inwards, with their H^+ occupying sites that Li^+ normally reside in $\text{Li}_x\text{Mn}_2\text{O}_4$. This is reasonable because the interior sites bracketed by O^{2-} ions should be electrostatically more favorable for cations and protons. In one instance, a type 1 hydroxyl group has abstracted a H^+ from a neighboring hydroxyl group to form a H_2O . The oxygen atom of that water molecule coordinates to a surface Mn ion 2.3 Å away in this snapshot, instead of the initial Mn-O ionic bonding distance (~ 1.9 Å). That Mn ion now has only 4 ionic bonds in addition to coordination to the H_2O molecule, and should be more susceptible to chemical reactions and dissolution. These trends are consistent with the experimental observations that protons accelerate decomposition of spinel $\text{Li}_x\text{Mn}_2\text{O}_4$.^{5,32,41} Despite the low temperature compared to experimental annealing conditions during synthesis,⁶⁹ evidence of H_2O loss is already observed.

Type 2 hydroxyl groups appear stable over the course of the AIMD trajectory. As surface O atoms dissolves after H^+ attacks, however, even Mn ions attached to type 2 hydroxyls may become undercoordinated, exposed, and susceptible to attack by other H_2O molecules or the organic electrolyte.

-
- ¹ *Advances in lithium-ion batteries*, edited by van Schalkwijk, W.A. & Scrosati, B. (Kluwer, New York, 2002).
- ² *Lithium-ion batteries: solid-electrolyte interphase*, edited by Wang Y.; Balbuena P.B. (Imperial College, London, 2004).
- ³ Xu, K. *Chem. Rev.* **2004**, *104*, 4304-4417.
- ⁴ Thackeray, M.M. *Prog. Solid State Chem.* **1997**, *25*, 1-71.
- ⁵ Thackeray, M.M.; Johnson, P.J.; de Picciotto, L.A.; Bruce, P.G.; Goodenough, J.B. *Mat. Res. Bull.* **1984**, *19*, 179-187.
- ⁶ Thackeray, M.M.; Shao-Horn, Y.; Kahaian, A.J.; Kepler, K.D.; Skinner, E.; Vaughey, J.T.; Hackney, S.A. *Electrchem. Solid State Lett.* **1998**, *1*, 7-9.
- ⁷ Ceder, G.; Van der Ven, A.; Aydinol, M.K. *J. Miner. Metals Mater. Soc.* **1998**, *50*, 35.
- ⁸ Wang, Y.; Nakamura, S.; Ue, M.; Balbuena, P.B. *J. Am. Chem. Soc.* **2001**, *123*, 11708-11718.
- ⁹ Han, Y.-K.; Lee, S.U. *Theor. Chem. Acc.* **2004**, *112*, 106-112.
- ¹⁰ Vollmer, J.M.; Curtiss, L.A.; Vissers, D.R.; Amine, K. *J. Electrochem. Soc.*, **2004**, *151*, A178-183.
- ¹¹ Leung, K.; Budzien, J.L. *Phys. Chem. Chem. Phys.* **2010**, *12*, 6583-6586.
- ¹² Yu, J.M.; Balbuena, P.B.; Budzien, J.L.; Leung, K. *J. Electrochem. Soc.* **2011**, *158*, A400-410.
- ¹³ Kim, S.-P.; van Duin, A.C.T.; Shenoy, V.B. *J. Power Sources* **2011**, *196*, 8590-8597.
- ¹⁴ Leung, K.; Qi, Y.; Zavadil, K.R.; Jung, Y.S.; Dillon, A.C.; Cavanagh, A.S.; Lee, S.H.; George, S.M. *J. Am. Chem. Soc.* **2011**, *133*, 14741-14754.
- ¹⁵ Aschauer, U.; Selloni, A. *Phys. Rev. Lett.* **2011**, *106*, 116102.
- ¹⁶ He, Y.B.; Tilocca, A.; Dulub, O.; Selloni, A.; Diebold, U. *Nature Mat.* **2009**, *8*, 585-589.
- ¹⁷ Vittadini, A.; Selloni, A.; Rotzinger, F.P.; Gratzel, M. *Phys. Rev. Lett.* **1998**, *81*, 2954-2957.
- ¹⁸ Sun, C.H.; Liu, L.M.; Selloni, A.; Lu, G.Q.; Smith, S.C. *J. Mater. Chem.* **2010**, *20*, 10319-10334.
- ¹⁹ Ufheil, J.; Würsig, A.; Schneider, O.D.; Novák, P. *Electrochim. Commun.* **2005**, *7* 1380-1384.
- ²⁰ Joho, F.; Novák, P. *Electrochim. Acta* **2000**, *45*, 3589-3599.
- ²¹ Simmen, F.; Foelske-Schmitz, A.; Verma, P.; Horisberger, M.; Lippert, Th.; Novák, P.; Schneider, C.W.; Wokaun, A. *Electrochim. Acta* **2011**, *56*, 8539-8544.
- ²² Eriksson, T.; Andersson, A.M.; Bishop, A.G.; Gejke, C.; Gustafsson, T.; Thomas, J.O. *J.*

- Electrochim. Soc.* **2002**, *149*, A69-78.
- ²³ Edström, K.; Gustafsson, T.; Thomas, J.O. *Electrochim. Acta* **2004**, *50*, 397-403.
- ²⁴ Matsushita, T.; Dokko, K.; Kanamura, K. *J. Power Sources* **2005**, *146*, 360-364.
- ²⁵ Kanamura, K.; Toriyama, S.; Shiraishi, S.; Ohashi, M.; Takehara Z. *J. Electroanal. Chem.* **1996**, *419*, 77-84.
- ²⁶ Kanamura, K.; Umegaki, T.; Ohashi, M.; Toriyama, S.; Shiraishi, S; Takehara, Z. *Electrochimica Acta* **2001**, *47*, 433-439.
- ²⁷ Matsuta, S.; Kato, Y.; Ota, T.; Kurokawa, H.; Yoshimura, S.; Fujitani, S. *J. Electrochim. Soc.* **2001**, *148*, A7-10.
- ²⁸ Aurbach, D.; Gamolsky, K.; Markovsky, B.; Salitra, G.; Gofer, Y.; Heider, U.; Oesten, R.; Schmidt, M. *J. Electrochim. Soc.* **2000**, *147*, 1322-1331.
- ²⁹ Aurbach, D.; Markovsky, B.; Levi, M.D.; Levi, E.; Schechter, A.; Moshkovich, M.; Cohen, Y. *J. Power Sources* **1999**, *81*, 95-111.
- ³⁰ Aurbach, D.; Levi, M.D.; Levi, E.; Teller, H.; Markovsky, B.; Salitra, G. Heider, U.; Heider, L. *J. Electrochim. Soc.* **1998**, *145*, 3024-3034.
- ³¹ Moshkovich, M.; Cojocaru, M.; Gottlieb, H.E.; Aurbach, D. *J. Electroanal. Chem.* **2001**, *497*, 84-96.
- ³² Jang, D.H.; Oh, S.M. *J. Electrochim. Soc.* **1997**, *144*, 3342-3348.
- ³³ Jang, D.H.; Shin, Y.J.; Oh, S.M. *J. Electrochim. Soc.* **1996**, *143*, 2204-2211.
- ³⁴ Yang, L.; Ravdel, B.; Lucht, B.L. *Electrochim. Solid State Lett.* **2010**, *13*, A95-97.
- ³⁵ Simmen, F.; Hintennach, A.; Horisberger, M.; Lippert, T.; Novák, P.; Schneider, C.W.; Wokaun, A. *J. Electrochim. Soc.* **2010**, *157*, A1026-1029.
- ³⁶ Würsig, A.; Buqa, H.; Holzapfel, M.; Krumeich, F.; Novák, P. *Electrochim. Solid-State Lett.* **2005**, *8*, A34-37.
- ³⁷ Imhof, R.; Novák, P. *J. Electrochim. Soc.* **1999**, *146*, 1702-1706.
- ³⁸ Guyomard, D.; Tarascon, J.M. *J. Electrochim. Soc.* **1993**, *140*, 3071-3081.
- ³⁹ Hirayama, M.; Ido, H.; Kim, K.S.; Cho, W.; Tamura, K.; Mizuki, J.; Kanno, R. *J. Am. Chem. Soc.* **2010**, *132*, 15268-15276.
- ⁴⁰ Hirayama, M.; Sonoyama, N.; Ito, M.; Minoura, M.; Mori, D.; Yamada, A.; Tamura, K.; Mizuki, J.; Kanno, R. *J. Electrochim. Soc.* **2007**, *154*, A1065-1072.
- ⁴¹ Du Pasquier, A.; Blyr, A.; Courjal, P.; Larcher, D.; Amatucci, G.; Gérand, B.; Tarason, J.-M.

- J. Electrochem. Soc.* **1999**, *146*, 428-436.
- ⁴² Matsuo, Y.; Kostecki, R.; McLarnon, F. *J. Electrochem. Soc.* **2001**, *148*, A687-692.
- ⁴³ Xia, Y.; Zhou, Y.; Yoshio, M. *J. Electrochem. Soc.* **1997**, *144*, 2593-2600.
- ⁴⁴ MacNeil, D.D.; Dahn, J.R. *J. Electrochem. Soc.* **2001**, *148*, A1211-1215.
- ⁴⁵ Amatucci, G.G.; Schmutz, C.N.; Blyr, A.; Sigala, C.; Gozdz, A.S.; Larcher, D.; Tarascon, J.M. *J. Power Sources* **1997**, *69*, 11-25.
- ⁴⁶ Xu, B.; Fell, C.R.; Chi, M.; Meng, Y.S. *Energy Environ. Sci.* **2011**, *4*, 2223-2233.
- ⁴⁷ Chen, Z.; Amine, K. *J. Electrochem. Soc.* **2006**, *153*, A316-320.
- ⁴⁸ Arakawa, M.; Yamaki, J. *J. Power Sources* **1995**, *54*, 250-254.
- ⁴⁹ Blyr, A.; Sigala, C.; Amatucci, G.; Guyomard, D.; Chabre, Y.; Tarascon, J.-M. *J. Electrochem. Soc.* **1998**, *145*, 194-209.
- ⁵⁰ Tsunekawa, H.; Tanimoto, S.; Marubayahsi, R.; Fujita, M.; Kifune, K.; Sano, M. *J. Electrochem. Soc.* **2002**, *149*, A1326-1331.
- ⁵¹ Amine, K.; Liu, J.; Kang, S.; Belharouak, I.; Huang, Y.; Vissers, D.; Henriksen, G. *J. Power Sources*, **2004**, *129*, 14-19.
- ⁵² Amine, K; Liu, J.; Belharouak, I.; Kang, S.-H.; Bloom. I.; Vissers, D.; Henriksen, G. *J. Power Sources*, **2005**, *146*, 111-115.
- ⁵³ Yang, L.; Takahashi, M.; Wang, B.F. *Electrochim. Acta* **2006**, *51*, 3228-3234.
- ⁵⁴ Hunter, J.C. *J. Solid State Chem.* **1981**, *39*, 142-147.
- ⁵⁵ Benedek, B.; Thackeray, M.M. *Phys. Rev. B* **2011**, *83*, 195439.
- ⁵⁶ Ouyang, C.Y.; Sljivancanin, Z.; Baldereschi, A. *Phys. Rev. B* **2009**, *79*, 235410.
- ⁵⁷ Maphangwa, R.R.; Parker, S.C.; Ngope, P.E. *Surf. Sci.* **2009**, *603*, 3184-3190.
- ⁵⁸ Balachandran, D.; Morgan, D.; Ceder, G.; van de Walle, A. *J. Solid State Chem.* **2003**, *173*, 462-475.
- ⁵⁹ Oxford, G.A.E.; Chaka, A.M. *J. Phys. Chem. C* **2011**, *115*, 16992-17008.
- ⁶⁰ Ue, M.; Murakami, A.; Nakamura, S. *J. Electrochem. Soc.* **2002**, *149*, A1572-1577.
- ⁶¹ Johansson, P. *J. Phys. Chem. A* **2006**, *110*, 12077-12080.
- ⁶² Zhang, X.R.; Pugh, J.K.; Ross, P.N. *J. Electrochm. Soc.* **2001**, *148*, E183-188.
- ⁶³ Xing, L.; Li, W.; Wang, C.; Gu, F.; Xu, M.; Tan, C.; Yi, J. *J. Phys. Chem. B* **2009**, *113*, 16596-16602.
- ⁶⁴ Xing, L.; Wang, C.; Li, W.; Xu, M.; Meng, X.; Zhao, S. *J. Phys. Chem. B* **2009**, *113*, 5181-5187.

- ⁶⁵ Xing, L.; Borodin, O.; Smith, G.; Li, W. *J. Phys. Chem.* **2011**, *115*, 13896-13905.
- ⁶⁶ Borodin, O.; Jow, T.R. *ECS Trans.* **2011**, *33*, 77-84.
- ⁶⁷ See a recent work on water-assisted Mn dissolution from the (100) surface: Benedek, R.; Thackeray, M.M.; Low, J.; Bucko, T. *J. Phys. Chem. C* **2012**, *116*, 4050-4059.
- ⁶⁸ The thermodynamics of acid-aided dissociation of bulk spinel $\text{Li}_x\text{Mn}_2\text{O}_4$ has also been predicted. See: Benedek, R.; Thackeray, M.M.; van de Walle, A. *J. Mater. Chem.* **2010**, *20*, 369-374; Benedek, R.; Thackeray, M.M.; van de Walle, A. *Chem. Mater.* **2008**, *20*, 5485-5490; Benedek, R.; van de Walle, A. *J. Electrochem. Soc.* **2008**, *155*, A711-715; Benedek, R.; Thackeray, M.M. *Electrochem. Solid State Lett.* **2006**, *9*, A265-267.
- ⁶⁹ Huang, M.-R.; Lin, C.-W.; Lu, H.-Y. *it Appl. Surf. Sci.* **2001**, *177*, 103-113.
- ⁷⁰ Car, R.; Parrinello M. *Phys. Rev. Lett.* **1985**, *55*, 2471-2474.
- ⁷¹ Kresse, G.; Furthmüller, J. *Phys. Rev. B* **1996**, *54*, 11169-11186, *Comput. Mater. Sci.* **1996**, *6*, 15-50.
- ⁷² Kresse G.; Joubert, D. *Phys. Rev. B* **1999**, *59*, 1758-1775.
- ⁷³ Perdew, J.P., Burke, K.; Ernzerhof, .M. *Phys. Rev. Lett.* **1996**, *77*, 3865-3868.
- ⁷⁴ Dudarev, S.L.; Botton, G.A.; Savrasov, S.Y.; Humphreys, C.J.; Sutton, A.P. *Phys. Rev. B* **1998**, *57*, 1505-1509.
- ⁷⁵ Zhou, F.; Cococcioni, M.; Marianetti, C.A.; Morgan, D.; Ceder, G. *Phys. Rev. B* **2004**, *70*, 235121.
- ⁷⁶ Heyd, J.; Scuseria, G.E.; Ernzerhof, M. *J. Chem. Phys.* **2003**, *118*, 8207-8215; Vydrov, O.A.; Scuseria, G.E.; Perdew, J.P. *J. Chem. Phys.* **2007**, *126*, 154109.
- ⁷⁷ Paier, J.; Marsman, M.; Kresse, G. *J. Chem. Phys.* **2007**, *127*, 024103.
- ⁷⁸ Henkelman, G.; Uberuaga, B.P.; Jonsson, H. *J. Chem. Phys.* **2000**, *113*, 9901-9904.
- ⁷⁹ Assary, R.S.; Curtiss, L.A.; Redfern, P.C.; Zhang, Z.C.; Amine, K. *J. Phys. Chem. C* **2011**, *115*, 12216-12223.
- ⁸⁰ Marzari, N.; Vanderbilt, D. *Phys. Rev. B* **1997**, *56*, 12847-12865.
- ⁸¹ Leung, K.; Nielsen, I.M.B.; Sai, N.; Medforth, C.J.; Shelnutt, J.A. *J. Phys. Chem. A* **2010**, *114*, 10174-10184.
- ⁸² Roy, L.E.; Jakubikova E.; Guthrie, M.G.; Batista E.R. *J. Phys. Chem. A* **2009**, *113*, 6745-6750.
- ⁸³ Galstyan, A; Knapp, E.W. *J. Comp. Chem.* **2009**, *30*, 203-211.
- ⁸⁴ Cramer, C.J.; Truhlar, D.G. *Phys. Chem. Chem. Phys.* **2009**, *11*, 10757-10816.

- ⁸⁵ The PBE functional used also underestimates dispersion forces between liquid EC and the cathode oxide. This can be corrected with empirical augmentations; see, e.g., Grimme, S. *J. Comp. Chem.* **2006**, *27*, 1787-1799.
- ⁸⁶ Laio, A.; Parrinello, M. *Proc. Natl. Acad. Sci. USA* **2002**, *99*, 12562-12566.
- ⁸⁷ Iannuzzi, M.; Laio, A.; Parrinello, M. *Phys. Rev. Lett.* **2003**, *90*, 238302.
- ⁸⁸ Laio, A.; Gervasio, F.L. *Rep. Prog. Phys.* **2008**, *71*, 126601.
- ⁸⁹ Geissler, P.L.; Dellago, C.; Chandler, D.; Hutter, J.; Parrinello, M. *Science*, **2001**, *291*, 2121-2124.
- ⁹⁰ Ouyang, C.; Du, Y.; Shi, S.; Lei, M. *Phys. Lett. A* **2009**, *373*, 2796-2799.

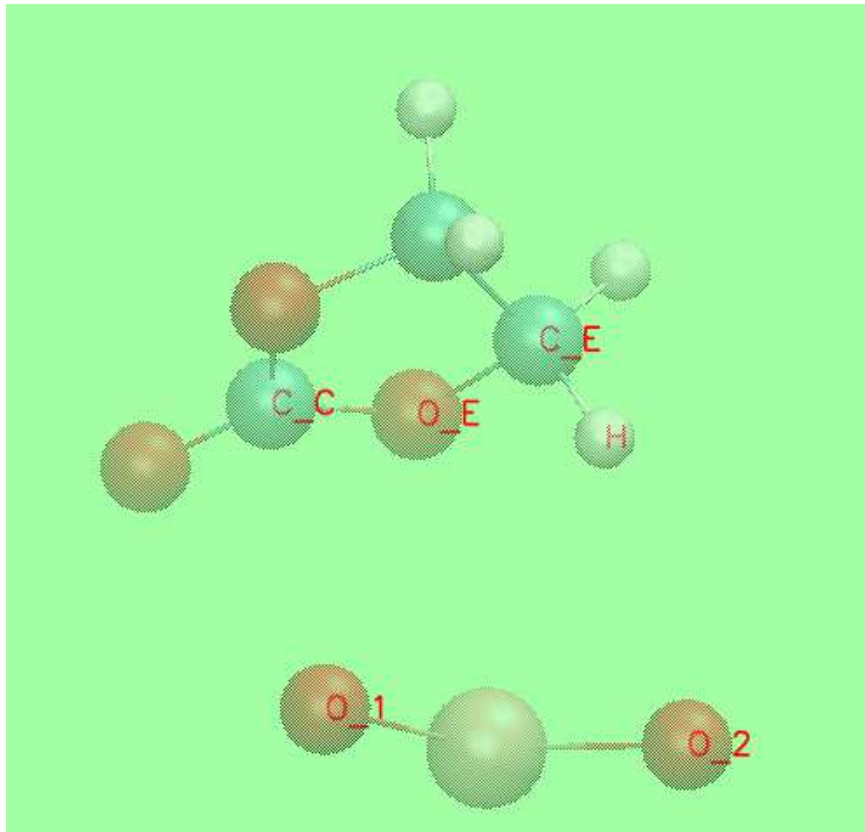


FIG. 1: Ethylene carbonate (EC) molecule. The panel depicts an isolated EC weakly bound to the surface; three $\text{Li}_x\text{Mn}_2\text{O}_4$ atoms are also depicted to explain the labeling scheme used in the text. Purple, dark blue, red, light blue, and white spheres represent Mn, Li, O, C, and H atoms, respectively.

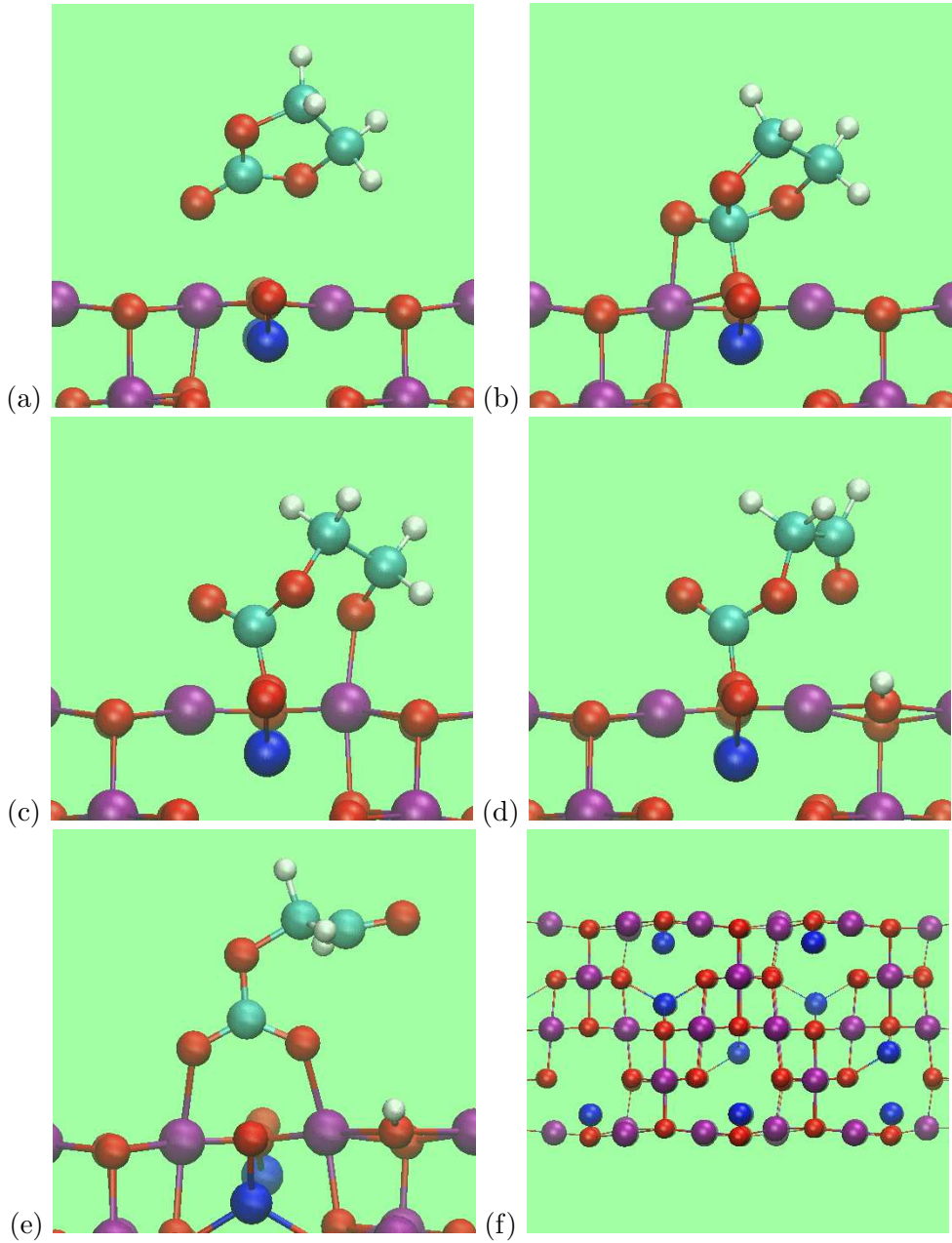


FIG. 2: (a) Intact EC (A) on $\text{Li}_{0.6}\text{Mn}_2\text{O}_4$ (100) surface. (b) Intermediate B. Note that the EC C_{C} atom sits atop a surface oxygen ion that is not bonded to a Mn immediately below. (c) Intermediate C, with a broken $\text{C}_{\text{C}}\text{-O}_{\text{E}}$ bond. The surface Mn(III) ion coordinated to the O_{E} now becomes a Mn(IV). (d) Intermediate D. A proton is transfer to a surface O ion. Two electrons are transferred; the surface Mn(IV) described in panel (c) reverts to a Mn(III). Configuration (d) reorganizes to (e) during AIMD simulations without further e^- transfer. (f) Most stable Li distribution in $\text{Li}_6\text{Mn}_{20}\text{O}_{40}$ (100) surface slab, viewed along the (011) direction, about 3 unit cells abreast.

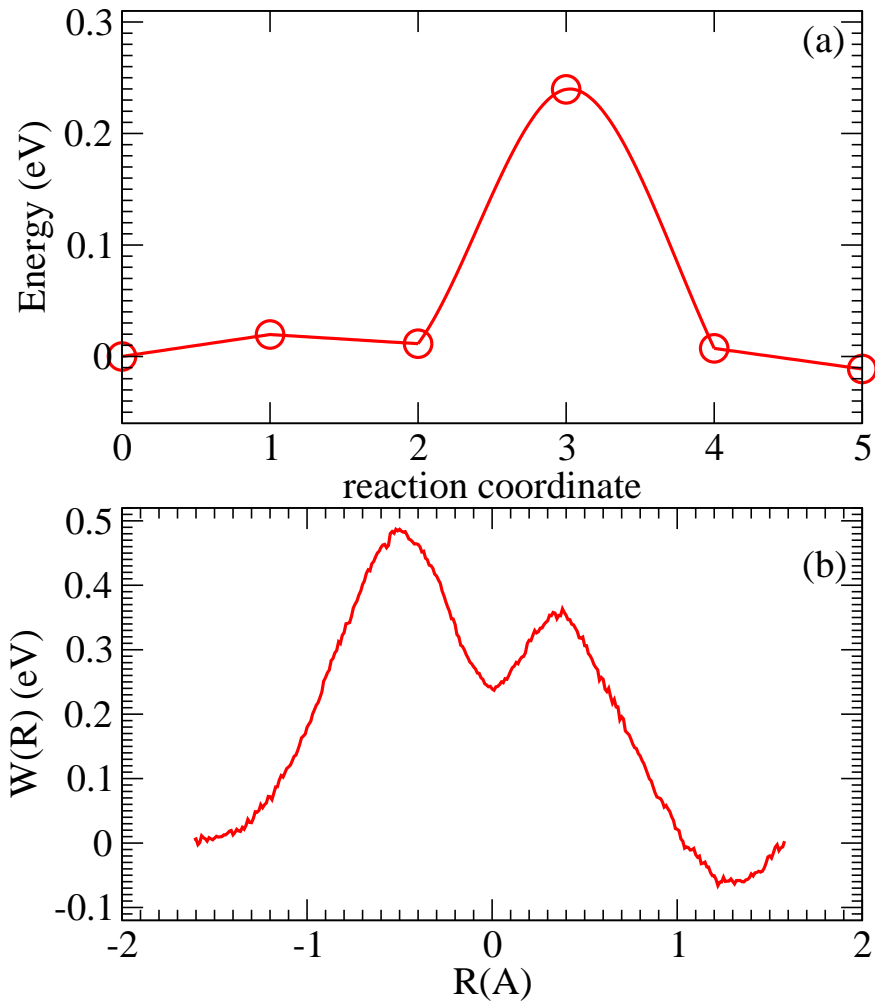


FIG. 3: (a) Energy profile linking configurations A and B, computed at T=0 K using the NEB method. (b) Potential-of-mean-force linking the A, B, and C free energy basins along the composite reaction coordinate R described in the text.

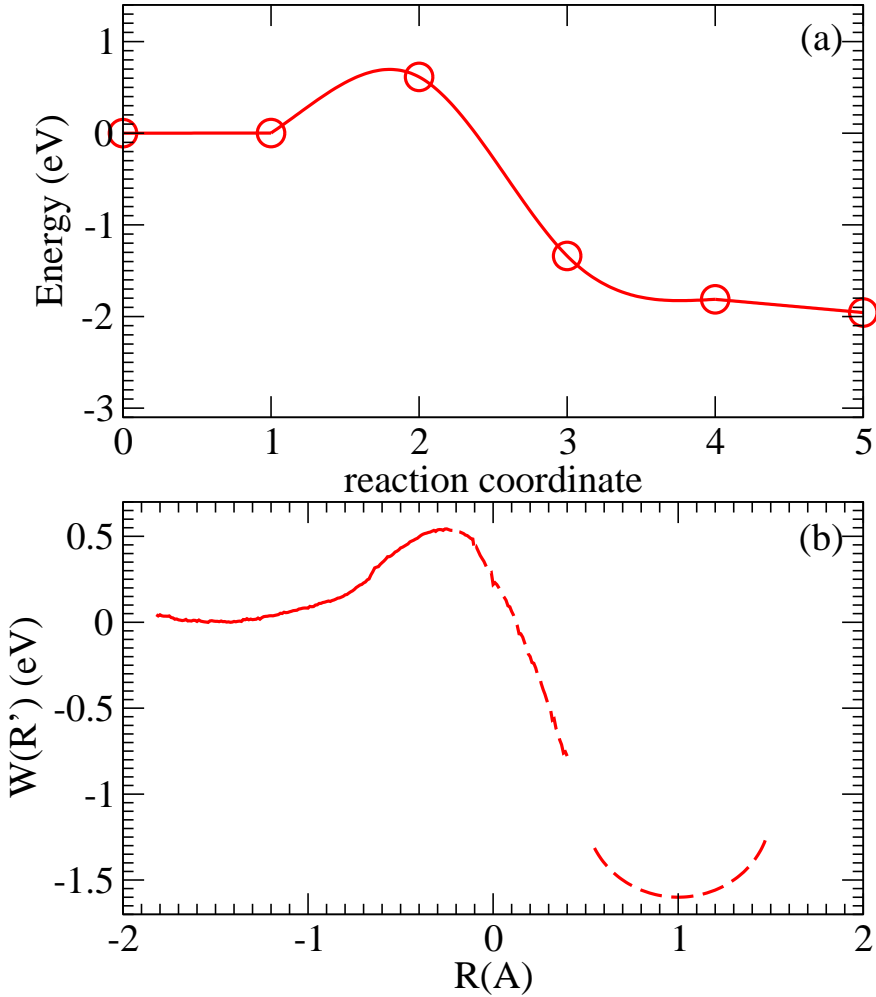


FIG. 4: (a) Energy profile linking configurations C and D, computed at $T=0$ K using the NEB method. (b) Potential-of-mean-force linking C and D along the composite reaction coordinate R' described in the text. In panel (b), the bottom of the well at $R=1$ Å has not been determined.

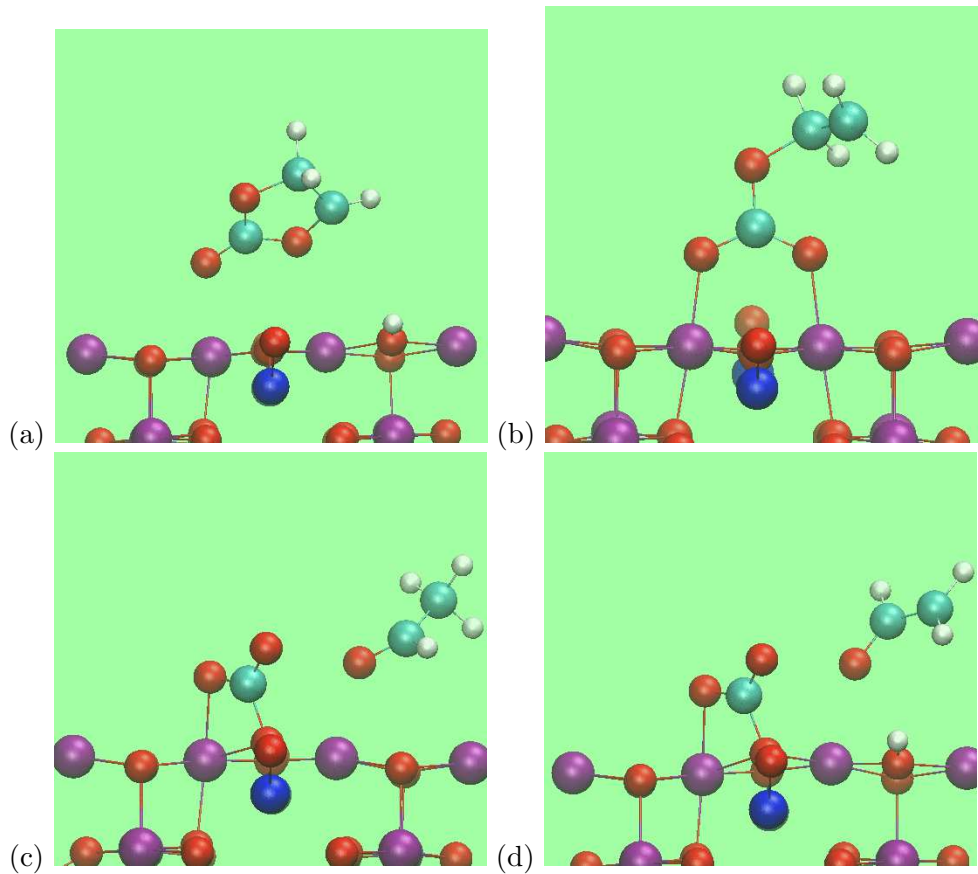


FIG. 5: Four decomposition products or intermediates not considered part of the main EC decomposition pathway, with zero temperature energies of +0.398 eV, +1.562 ev, -0.646 eV, and -0.376 eV relative to Fig. 2a, respectively.

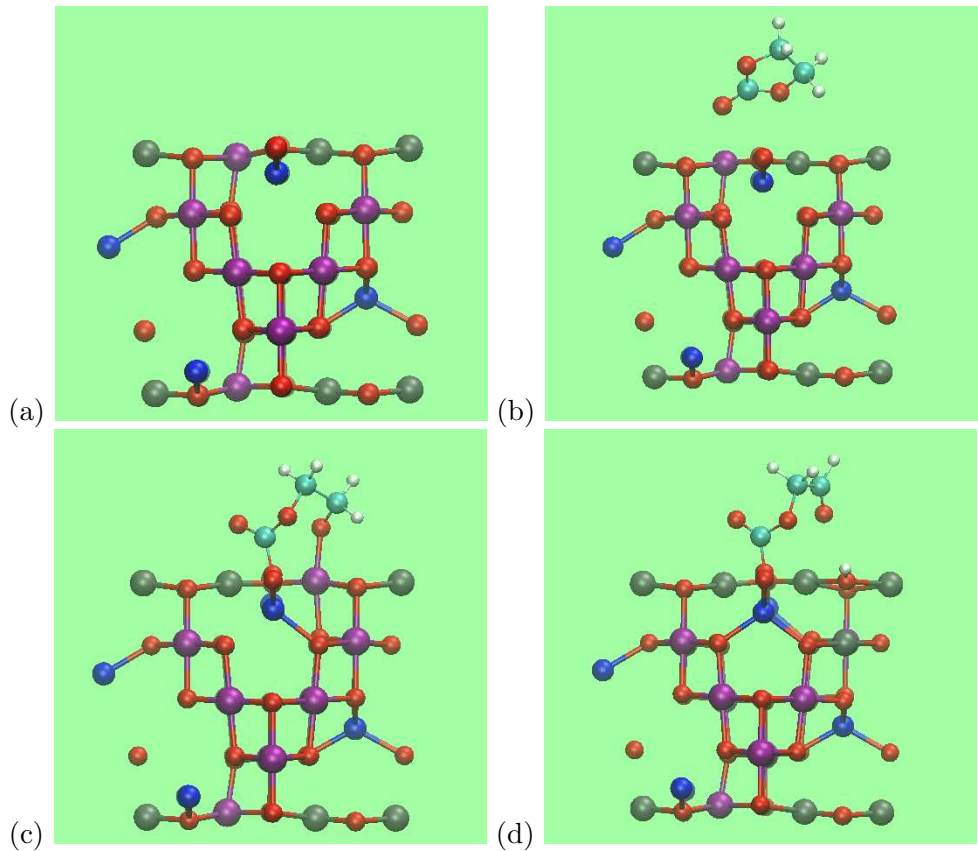


FIG. 6: Magnetic moments of Mn ions corresponding to the bare $\text{Li}_{0.6}\text{Mn}_2\text{O}_4$ slab, intact EC (Fig. 2a), EC with a broken C-O bond (Fig. 2c), and oxidized EC (Fig. 2d). Purple and dark-green spheres represent Mn(IV) and Mn(III), respectively.

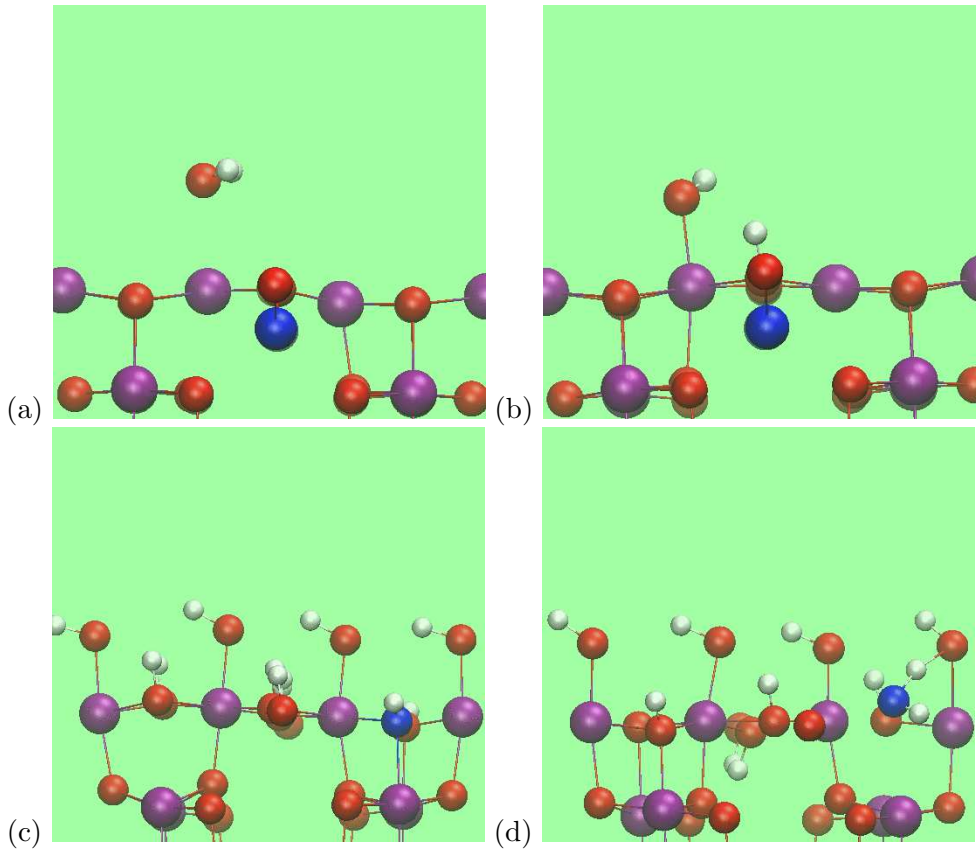


FIG. 7: (a)&(b): Intact and dissociated H₂O molecule on MnO₂ surface. In panel (a), one of the water protons is obscured by the O atom. (c)&(d): The initial and final hydroxylated and protonated MnO₂ (100) surface configurations along an AIMD trajectory, respectively. In panel (d), one OH group on the surface has abstracted a proton from another hydroxyl group and has turned into a H₂O molecule; that oxygen is colored deep blue.